

43210, USA. <sup>12</sup>Istituto Nazionale di Fisica Nucleare, Sezione di Perugia, I-06123 Perugia, Italy. <sup>13</sup>Dipartimento di Fisica, Università degli Studi di Perugia, I-06123 Perugia, Italy. <sup>14</sup>Dipartimento di Fisica "M. Merlin" dell'Università e del Politecnico di Bari, I-70126 Bari, Italy. <sup>15</sup>Istituto Nazionale di Fisica Nucleare, Sezione di Bari, 70126 Bari, Italy. <sup>16</sup>Laboratoire Leprince-Ringuet, École polytechnique, CNRS/IN2P3, Palaiseau, France. <sup>17</sup>Department of Physics, University of Washington, Seattle, WA 98195–1560, USA. <sup>18</sup>Institut de Ciències de l'Espai (IEEC-CSIC), Campus UAB, 08193 Barcelona, Spain. <sup>19</sup>Istituto Nazionale di Astrofisica (INAF)–Istituto di Astrofisica Spaziale e Fisica Cosmica, I-20133 Milano, Italy. <sup>20</sup>Agenzia Spaziale Italiana Science Data Center, I-00044 Frascati (Roma), Italy. <sup>21</sup>NASA Goddard Space Flight Center, Greenbelt, MD 20771, USA. <sup>22</sup>Center for Research and Exploration in Space Science and Technology and NASA Goddard Space Flight Center, Greenbelt, MD 20771, USA. <sup>23</sup>Department of Physics and Center for Space Sciences and Technology, University of Maryland Baltimore County, Baltimore, MD 21250, USA. <sup>24</sup>George Mason University, Fairfax, VA 22030, USA. <sup>25</sup>Laboratoire de Physique Théorique et Astroparticules, Université Montpellier 2, CNRS/IN2P3, Montpellier, France. <sup>26</sup>Department of Physics and Astronomy, Sonoma State University, Rohnert Park, CA 94928–3609, USA. <sup>27</sup>Department of Physics, Stockholm University, AlbaNova, SE-106 91 Stockholm, Sweden. <sup>28</sup>The Oskar Klein Centre for Cosmoparticle Physics, AlbaNova, SE-106 91 Stockholm, Sweden. <sup>29</sup>Dipartimento di Fisica, Università di Udine and Istituto Nazionale di Fisica Nucleare, Sezione di Trieste, Gruppo Col-

legato di Udine, I-33100 Udine, Italy. <sup>30</sup>Université de Bordeaux, Centre d'Études Nucléaires Bordeaux Gradignan, UMR 5797, Gradignan, 33175, France. <sup>31</sup>CNRS/IN2P3, Centre d'Études Nucléaires Bordeaux Gradignan, UMR 5797, Gradignan, 33175, France. <sup>32</sup>Department of Physical Sciences, Hiroshima University, Higashi-Hiroshima, Hiroshima 739-8526, Japan. <sup>33</sup>Department of Astronomy and Astrophysics, Pennsylvania State University, University Park, PA 16802, USA. <sup>34</sup>Department of Physics and Department of Astronomy, University of Maryland, College Park, MD 20742, USA. <sup>35</sup>INAF Istituto di Radioastronomia, 40129 Bologna, Italy. <sup>36</sup>Max-Planck-Institut für Radioastronomie, Auf dem Hügel 69, 53121 Bonn, Germany. <sup>37</sup>Center for Space Plasma and Aeronomic Research, University of Alabama in Huntsville, Huntsville, AL 35899, USA. <sup>38</sup>Department of Physics, Royal Institute of Technology, AlbaNova, SE-106 91 Stockholm, Sweden. <sup>39</sup>Waseda University, 1-104 Totsukamachi, Shinjuku-ku, Tokyo, 169-8050, Japan. <sup>40</sup>Department of Physics, Tokyo Institute of Technology, Meguro City, Tokyo 152-8551, Japan. <sup>41</sup>Cosmic Radiation Laboratory, Institute of Physical and Chemical Research (RIKEN), Wako, Saitama 351-0198, Japan. <sup>42</sup>Centre d'Étude Spatiale des Rayonnements, CNRS/UPS, BP 44346, F-30128 Toulouse Cedex 4, France. <sup>43</sup>Istituto Nazionale di Fisica Nucleare, Sezione di Roma "Tor Vergata," I-00133 Roma, Italy. <sup>44</sup>Department of Physics and Astronomy, University of Denver, Denver, CO 80208, USA. <sup>45</sup>Max-Planck Institut für Extraterrestrische Physik, 85748 Garching, Germany. <sup>46</sup>Institut für Astro- und Teilchenphysik and Institut für Theoretische Physik, Leopold-Franzens-Universität Innsbruck, A-6020 Innsbruck,

Austria. <sup>47</sup>Space Sciences Division, NASA Ames Research Center, Moffett Field, CA 94035–1000, USA. <sup>48</sup>NYCB Real-Time Computing, Lattingtown, NY 11560–1025, USA. <sup>49</sup>Astronomical Observatory, Jagiellonian University, 30-244 Kraków, Poland. <sup>50</sup>Department of Chemistry and Physics, Purdue University Calumet, Hammond, IN 46323–2094, USA. <sup>51</sup>Institute of Space and Astronautical Science, Japanese Aerospace Exploration Agency, 3-1-1 Yoshinodai, Sagami-hara, Kanagawa 229-8510, Japan. <sup>52</sup>Institució Catalana de Recerca i Estudis Avançats, Barcelona, Spain. <sup>53</sup>Consorzio Interuniversitario per la Fisica Spaziale, I-10133 Torino, Italy. <sup>54</sup>Dipartimento di Fisica, Università di Roma "Tor Vergata," I-00133 Roma, Italy. <sup>55</sup>School of Pure and Applied Natural Sciences, University of Kalmar, SE-391 82 Kalmar, Sweden. <sup>56</sup>Centre for Astrophysics Research, University of Hertfordshire, College Lane, Hatfield AL10 9AB, UK.

**Supporting Online Material**

www.sciencemag.org/cgi/content/full/science.1184656/DC1  
Materials and Methods

SOM Text

Figs. S1 to S3

Tables S1 to S3

References

13 November 2009; accepted 19 March 2010

Published online 1 April 2010;

10.1126/science.1184656

Include this information when citing this paper.

# The Equation of State of a Low-Temperature Fermi Gas with Tunable Interactions

N. Navon,\*† S. Nascimbène,\* F. Chevy, C. Salomon

Interacting fermions are ubiquitous in nature, and understanding their thermodynamics is an important problem. We measured the equation of state of a two-component ultracold Fermi gas for a wide range of interaction strengths at low temperature. A detailed comparison with theories including Monte-Carlo calculations and the Lee-Huang-Yang corrections for low-density bosonic and fermionic superfluids is presented. The low-temperature phase diagram of the spin-imbalanced gas reveals Fermi liquid behavior of the partially polarized normal phase for all but the weakest interactions. Our results provide a benchmark for many-body theories and are relevant to other fermionic systems such as the crust of neutron stars.

Recently, ultracold atomic Fermi gases have become a tool of choice to study strongly correlated quantum systems because of their high controllability, purity, and tunability of interactions ( $I$ ). In the zero-range limit, interactions in a degenerate Fermi system with two spin-components are completely characterized by a single parameter  $1/k_F a$ , where  $a$  is the  $s$ -wave scattering length and  $k_F = (6\pi^2 n)^{1/3}$  is the Fermi momentum ( $n$  is the density per spin state). In cold atom gases, the value of  $|a|$  can be tuned over several orders of magnitude using a Feshbach resonance; this offers an opportunity to entirely explore the so-called BCS-BEC crossover, that is, the smooth transition from Bardeen-Cooper-Schrieffer (BCS) superfluidity at small

negative values of  $a$  to molecular Bose-Einstein Condensation (BEC) at small positive values of  $a$  ( $I$ , 2). Between these two well-understood limiting situations,  $a$  diverges, leading to strong quantum correlations. The description of this system is a challenge for many-body theories, as testified by the large amount of work in recent years ( $I$ ). The physics of the BEC-BCS crossover is relevant for very different systems, ranging from neutron stars to heavy nuclei and superconductors.

In the grand-canonical ensemble and at zero temperature, dimensional analysis shows that the Equation of State (EoS) of a two-component Fermi gas, relating the pressure  $P$  to the chemical potentials  $\mu_1$  and  $\mu_2$  of the spin components can be written as

$$P(\mu_1, \mu_2, a) = P_0(\mu_1) h \left( \delta_1 \equiv \frac{\hbar}{\sqrt{2m\mu_1} a}, \eta \equiv \frac{\mu_2}{\mu_1} \right) \quad (1)$$

where  $P_0(\mu_1) = 1/15\pi^2 (2m/\hbar^2)^{3/2} \mu_1^{5/2}$  is the pressure of a single-component ideal Fermi gas,

$m$  is the atom mass,  $\hbar$  is the Planck constant divided by  $2\pi$ , and  $\delta_1$  is the grand-canonical analog of the dimensionless interaction parameter  $1/k_F a$ . The indices 1 and 2 refer to the majority and minority spin components, respectively. From the dimensionless function  $h(\delta_1, \eta)$ , it is possible to deduce all the thermodynamic properties of the gas, such as the compressibility, the magnetization, or the existence of phase transitions. The aim of this paper is to measure  $h(\delta_1, \eta)$  for a range of interactions ( $\delta_1$ ) and spin imbalances ( $\eta$ ) and discuss its physical content. Because it contains the same information as Eq. 1, the function  $h$  will also be referred to as the EoS in the rest of the text.

In situ absorption images of harmonically trapped gases are particularly suited to investigate the EoS, as first demonstrated in (3) and (4). In the particular case of the grand-canonical ensemble, a simple formula relates the local pressure  $P$  at a distance  $z$  from the center of the trap along the  $z$  axis to the doubly integrated density profiles  $\bar{n}_1$  and  $\bar{n}_2$  (5).

$$P(\mu_1(z), \mu_2(z), a) = \frac{m\omega_r^2}{2\pi} (\bar{n}_1(z) + \bar{n}_2(z)) \quad (2)$$

Here, we define the local chemical potentials  $\mu_i(z) = \mu_i^0 - \frac{1}{2} m\omega_z^2 z^2$ , where  $\mu_i^0$  is the chemical potential of the component  $i$  at the bottom of the trap, assuming local density approximation.  $\omega_r$  and  $\omega_z$  are the transverse and axial angular frequencies of a cylindrically symmetric trap, respectively, and  $\bar{n}_i(z) = \int n_i(x, y, z) dx dy$  is the atomic density  $n_i$  of the component  $i$ , doubly integrated over the transverse  $x$  and  $y$  directions. In a single experimental run at a given magnetic field, two images are recorded, providing  $\bar{n}_1(z)$  and  $\bar{n}_2(z)$  (fig. S4); the  $z$ -dependence of the chemical potentials then enables the measurement of  $P$  along a curve in the  $(\delta_1, \eta)$  plane (6). This method was validated in (4) for the particular case of the

Laboratoire Kastler Brossel, CNRS, Université Pierre et Marie Curie, École Normale Supérieure, 24 rue Lhomond, 75231 Paris, France.

\*These authors contributed equally to this work.

†To whom correspondence should be addressed. E-mail: navon@ens.fr

unitary limit  $a = \infty$ . Deducing the function  $h$  from the doubly integrated profiles further requires a precise calibration of  $\omega_z$  and the knowledge of the central chemical potentials  $\mu_i^0$  (6).

Our experimental setup is presented in (7). We prepared an imbalanced mixture of  $^6\text{Li}$  in the two lowest internal spin states, at the magnetic field of 834 G (where  $a = \infty$ ), and trapped it in a hybrid magnetic-optical dipole trap. We then performed evaporative cooling by lowering the optical trap power, while the magnetic field was ramped to the final desired value for  $a$ . The cloud typically contained  $N = 2$  to  $10 \times 10^4$  atoms in each spin state at a temperature of  $0.03(3) T_F$ , justifying our  $T = 0$  assumption (6). The final trap frequencies are  $\omega_x/2\pi \sim 30$  Hz and  $\omega_r/2\pi \sim 1$  kHz. Below a critical spin population imbalance, our atomic sample consists of a fully paired superfluid occupying the center of the trap, surrounded by a normal mixed phase and an outer rim of an ideal gas of majority component atoms (4, 7, 8).

For a given magnetic field, 10 to 20 images are taken, leading after averaging to a low-noise EoS along one line in the  $(\delta_1, \eta)$  plane. Measurements at different magnetic fields chosen between 766 G and 981 G give a sampling of the surface  $h(\delta_1, \eta)$  in the range  $-1 < \delta_1 < 0.6$  and  $-2 < \eta < 0.7$  (Fig. 1). Let  $A(\delta_1)$  be the limiting value of the ratio of chemical potentials  $\mu_1(z)/\mu_2(z)$  below which the minority density vanishes. At fixed  $\delta_1$  and  $\eta < A(\delta_1)$ ,  $h(\delta_1, \eta)$  represents the EoS of an ideal Fermi gas of majority atoms and is equal to 1. For  $\eta > A(\delta_1)$ , it slowly rises and corresponds to the normal mixed phase, where both spin components are present. At a critical value  $\eta = \eta_c(\delta_1)$ , the slope of  $h$  abruptly changes (6), the signature of a first-order phase transition from the normal phase (for  $A < \eta < \eta_c$ ) to a superfluid phase with a lower chemical potential imbalance ( $\eta > \eta_c$ ). We notice that the discontinuity is present for all values of  $\delta_1$  we investigated, and this feature is more pronounced on the BEC side.

Let us first consider the EoS of the superfluid phase,  $\eta > \eta_c$ . Each of our in situ images has, along the  $z$  axis, values of the chemical potential ratio  $\eta(z) = \mu_2(z)/\mu_1(z)$  both lower and greater than  $\eta_c$ . In the region where  $\eta(z) > \eta_c$ , the doubly integrated density difference  $\bar{n}_1(z) - \bar{n}_2(z)$  is constant within our signal-to-noise ratio (fig. S4). This is the signature of equal densities of the two species in the superfluid core, that is, the superfluid is fully paired. Using Gibbs-Duhem relation  $n_i = \frac{\partial P}{\partial \mu_i}$ , equal densities  $n_1 = n_2$  imply that  $P(\mu_1, \mu_2, a)$  is a function of  $\mu$  and  $a$  only, where  $\mu \equiv (\mu_1 + \mu_2)/2$ . For the balanced superfluid, we then write the EoS symmetrically.

$$P(\mu_1, \mu_2, a) = 2P_0(\tilde{\mu})h_S \left( \tilde{\delta} \equiv \frac{\hbar}{\sqrt{2m\tilde{\mu}a}} \right) \quad (3)$$

To avoid using negative chemical potentials, we define here  $\tilde{\mu} = \mu - E_b/2$ , where  $E_b$  is the molecular binding energy  $E_b = -\hbar^2/ma^2$  for  $a > 0$  (and 0 for  $a \leq 0$ ).  $h_S(\tilde{\delta})$  is then a single-variable function. It fully describes the ground-state

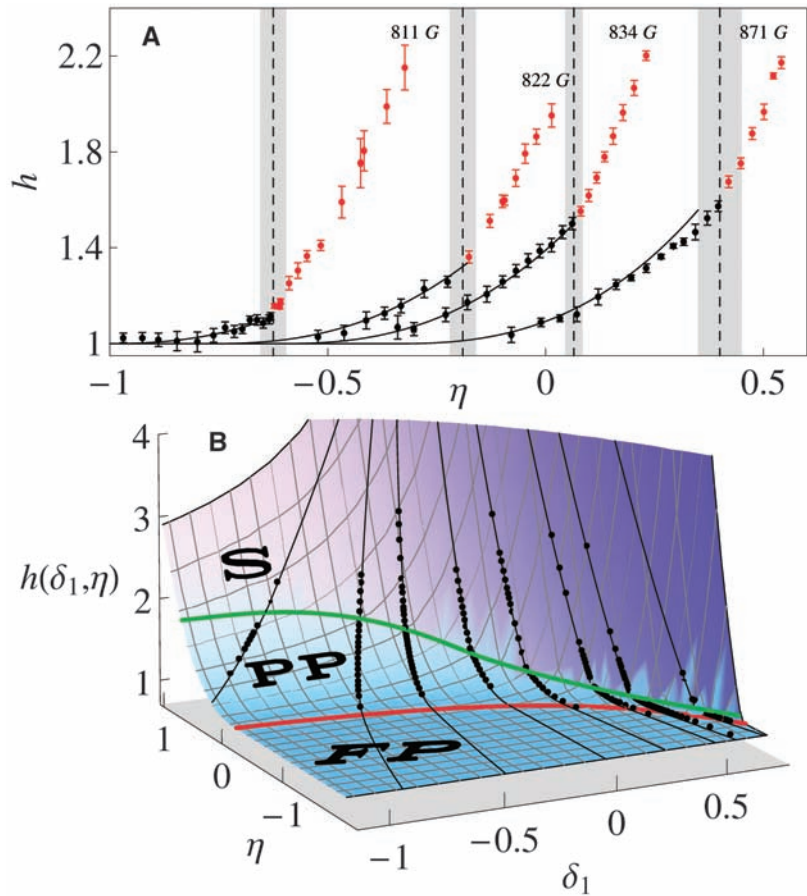


**Fig. 1.**  $h(\delta_1, \eta)$  of a zero-temperature two-component Fermi gas in the BEC-BCS crossover. **(A)** Samples of the data for different magnetic fields. The black (red) data points correspond to the normal (superfluid) phase and are separated at  $\eta_c(\delta_1)$  by a clear kink in the local slope of  $h$ . Solid black lines are the predictions of the polaron ideal gas model (Eq. 8). The scattering length corresponding to each curve is (from left to right): (1.7, 3.4,  $\infty$ , and  $-1.3$ ) in units of  $10^4 a_0$ , where  $a_0$  is the Bohr radius. **(B)**  $h(\delta_1, \eta)$ . The black dots are data recorded for each magnetic field value (as in Fig. 1A). The black lines correspond to the parametric curves  $[\delta_1(\eta), \eta]$  scanned by the density inhomogeneity in the harmonic trap (6). The red line is  $A(\delta_1)$ , the frontier between the fully polarized (FP) ideal gas  $h = 1$  and the normal partially polarized (PP) phase. The green line is  $\eta_c(\delta_1)$ , marking the phase transition between the normal and superfluid (S) phases. The surface is the parametrization of  $h(\delta_1, \eta)$  given in the text.

**Fig. 2.**  $h_S(\tilde{\delta})$  of the  $T = 0$  balanced superfluid in the BEC-BCS crossover (black dots). The blue solid line is the fit  $h_S^{\text{BCS}}(\tilde{\delta})$  on the BCS side of the resonance; the red solid line is the fit  $h_S^{\text{BEC}}(\tilde{\delta})$  on the BEC side. The dotted (dashed) red line is the mean-field (LHY) theory (32). (Inset) Zoom on the BCS side. The dotted and dashed blue lines are the EoS, including the mean-field and LHY terms, respectively. The systematic uncertainties on the  $x$  and  $y$  axes are about 5%. The errors bars represent the standard deviation of the statistical uncertainty.

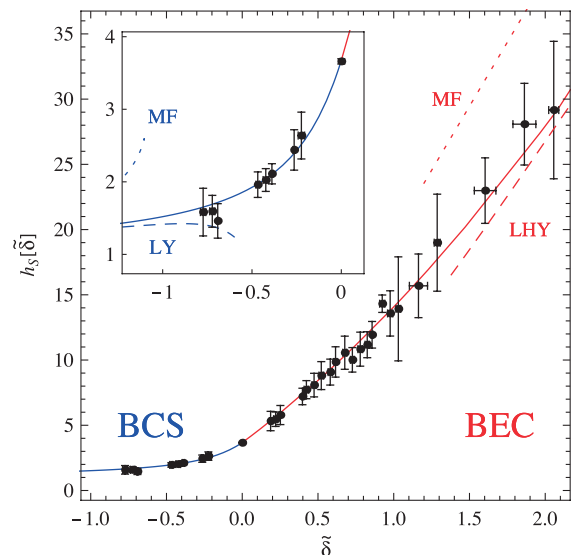
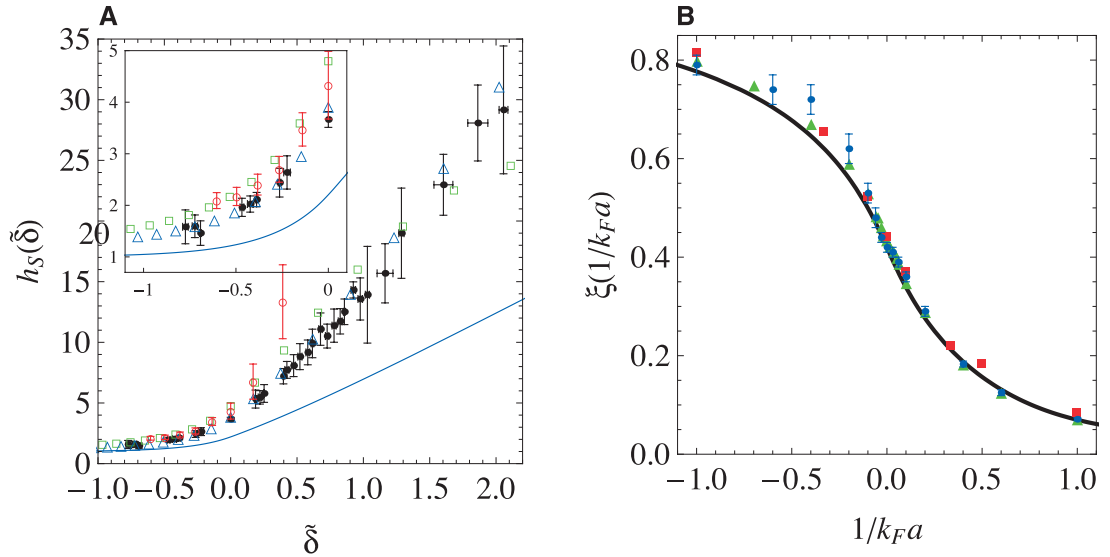


**Fig. 3.** Comparison with many-body theories. **(A)** Direct comparison of  $h_S(\tilde{\delta})$  with a quantum Monte-Carlo calculation [red open circles (22)], a diagrammatic method [green open squares (23)], a Nozières-Schmitt-Rink approximation [blue open triangles (21)], and the BCS mean-field theory (solid blue line). (Inset) Zoom on the BCS side. **(B)** EoS in the canonical ensemble  $\xi(1/k_F a)$  (solid black line) deduced from the Padé-type approximants to the experimental data  $h_S^{\text{BCS}}$  and  $h_S^{\text{BEC}}$  plotted in Fig. 2. Fixed-Node Monte-Carlo theories: red squares (24), blue circles (25), and green triangles (26).



macroscopic properties of the balanced superfluid in the BEC-BCS crossover and is displayed in Fig. 2 as black dots.

To extract relevant physical quantities, such as beyond mean-field corrections, it is convenient to parametrize our data with analytic functions. In this pursuit, we use Padé-type approximants (6), interpolating between the EoS measured around unitarity and the well-known mean-field expansions on the BEC and BCS limits. The two analytic functions,  $h_S^{\text{BCS}}$  and  $h_S^{\text{BEC}}$ , are respectively represented in blue and red solid lines in Fig. 2 and represent our best estimate of the EoS in the whole BEC-BCS crossover.

On the BCS side,  $(\tilde{\delta}) < 0$ ,  $h_S^{\text{BCS}}$  yields the following perturbative expansion of the energy in series of  $k_F a$

$$E = \frac{3}{5} N E_F \left( 1 + \frac{10}{9\pi} k_F a + 0.18(2)(k_F a)^2 + 0.03(2)(k_F a)^3 + \dots \right) \quad (4)$$

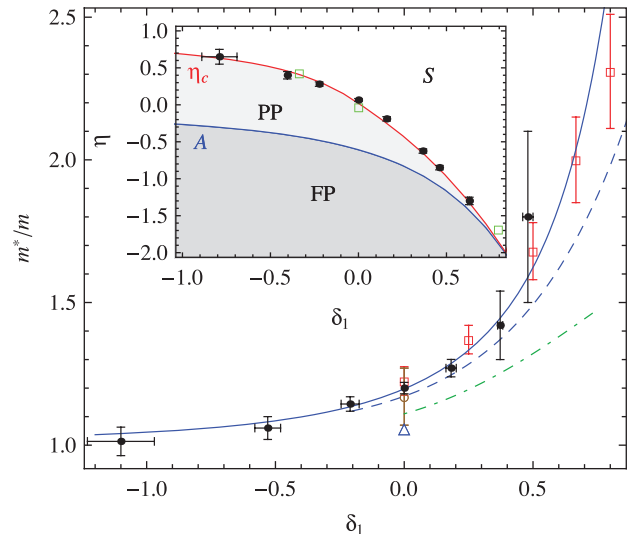
where  $N$  is the total number of atoms,  $E_F$  is the Fermi energy, and where by construction of  $h_S^{\text{BCS}}$ , the mean-field term (proportional to  $k_F a$ ) is fixed to its exact value  $10/9\pi$ . We obtain beyond mean-field corrections up to the third order. The term proportional to  $(k_F a)^2$  agrees with the Lee-Yang (9, 10) theoretical calculation  $4(11-2\log 2)/21\pi^2 \approx 0.186$ . The third-order coefficient also agrees with the value 0.030 computed in (11).

Around unitarity, the energy expansion yields

$$E = \frac{3}{5} N E_F \left( \xi_s - \zeta \frac{1}{k_F a} + \dots \right) \quad (5)$$

We find the universal parameter of the unitary  $T = 0$  superfluid,  $\xi_s = 0.41(1)$  with 2% accuracy. This value is in agreement with recent calculations and measurements (1). Our thermodynamic measurement  $\zeta = 0.93(5)$  can be compared with a recent experimental value  $\zeta = 0.91(4)$  (12), as well as the theoretical value  $\zeta = 0.95$  (13), both of them

**Fig. 4.** Effective mass  $m^*/m$  of the polaron in the BEC-BCS crossover (black dots). The blue dashed line is a calculation from (29), red open squares (30), green dot-dashed line (26), and blue solid line (31). Measurements at unitarity through density profile analysis [blue triangle (3)] and collective modes study [brown empty circle (7)] are also displayed. (Inset) Phase diagram of a zero-temperature imbalanced Fermi gas in the BEC-BCS crossover. The blue line is the theoretical value of  $A$  (26, 29, 30) that sets the separation between the partially polarized (PP) and the fully polarized (FP) phases. Black dots are the measured values of  $\eta_c$  (as in Fig. 1A), which set the separation between the superfluid (S) phase and the partially polarized phase. The red line is the calculation of  $\eta_c$  using our EoS of the superfluid and the model (Eq. 8) for the normal phase. The green squares are lower bounds of  $\eta_c$  given by the values of the gap measured in (33); see (6).



obtained through the study of the pair correlation function. This experimental agreement confirms the link between the macroscopic thermodynamic properties and the microscopic short-range pair correlations, as shown theoretically in (14).

In the BEC limit, the energy of the superfluid is that of a weakly interacting Bose-Einstein condensate of molecules (9, 15)

$$E = \frac{N}{2} E_b + N \frac{\pi \hbar^2 a_{dd}}{2m} \times n \left( 1 + \frac{128}{15\sqrt{\pi}} \sqrt{na_{dd}^3} + \dots \right) \quad (6)$$

where  $a_{dd} = 0.6a$  is the dimer-dimer scattering length ( $l$ ) and  $n$  is the dimer density. The term in  $\sqrt{na_{dd}^3}$  is the well-known Lee-Huang-Yang (LHY) correction to the mean-field interaction

between molecules (9, 15). Signatures of beyond mean-field effects were previously observed through a pioneering study of collective modes (16) and density profile analysis (17), but no quantitative comparison with Eq. 6 was made. Fitting our data in the deep BEC regime with Eq. 6, we measure the bosonic LHY coefficient  $4.4(5)$ , in agreement with the exact value  $128/15\sqrt{\pi} \approx 4.81$  calculated for elementary bosons in (9) and recently for composite bosons in (15).

Having checked this important beyond mean-field contribution, we can go one step further in the expansion. The analogy with point-like bosons suggests that the next term should be written as  $[\frac{8}{3}(4\pi - 3\sqrt{3})na_{dd}^3(\log(na_{dd}^3) + B)]$  (6, 18, 19). Using  $h_S^{\text{BEC}}(\tilde{\delta})$  (Fig. 2) (6), we deduce the effective three-body parameter for composite bosons  $B = 7(1)$ . Interestingly, this value is close

to the bosonic hard-sphere calculation  $B = 8.5$  (20) and to the value  $B \approx 7.2$  for point-like bosons with large scattering length (19).

Our measurements also allow direct comparison with advanced many-body theories developed for homogeneous gases in the strongly correlated regime. As displayed in Fig. 3A, our data are in agreement with a Nozières-Schmitt-Rink approximation (21) but show significant differences from a quantum Monte-Carlo calculation (22) and a diagrammatic approach (23). The measured EoS strongly disfavors the prediction of BCS mean-field theory.

Comparison with Fixed-Node Monte-Carlo theories requires the calculation of the EoS  $\xi(1/k_F a)$  in the canonical ensemble

$$\xi\left(\frac{1}{k_F a}\right) \equiv \frac{E - \frac{N}{2}E_b}{\frac{3}{5}NE_F} \quad (7)$$

that is deduced from  $h_S^{\text{BCS}}(\tilde{\delta})$  and  $h_S^{\text{BEC}}(\tilde{\delta})$  (6). As shown in Fig. 3B, the agreement with theories (24–26) is very good.

We now discuss the EoS of the partially polarized normal phase (black points in Fig. 1). At low concentrations, we expect the minority atoms to behave as noninteracting quasiparticles, the fermionic polarons (27). The polarons are dressed by the majority Fermi sea through a renormalized chemical potential  $\mu_2 - A(\delta_1)\mu_1$  (28) and an effective mass  $m^*(\delta_1)$  (26, 29, 30). Following a Fermi liquid picture, we propose to express the gas pressure as the sum of the Fermi pressure of the bare majority atoms and of the polarons (4).

$$h(\delta_1, \eta) = 1 + \left(\frac{m^*(\delta_1)}{m}\right)^{3/2} (\eta - A(\delta_1))^{5/2} \quad (8)$$

Our measured EoS agrees with this model at unitarity and on the BEC side of the resonance (Fig. 1), where for  $m^*(\delta_1)$  we use the calculations from (30, 31). On the BCS side of the resonance, however, we observe at large minority concentrations an intriguing deviation to Eq. 8. In the BCS regime, the superfluid is less robust to spin imbalance. Consequently, the ratio of the two densities  $n_1/n_2$  in the normal phase becomes close to unity near the superfluid/normal boundary  $\eta_c$ . The polaron ideal gas picture then fails.

Alternatively, we can let the effective mass  $m^*$  be a free parameter in the model in Eq. 8 in the fit of our data around  $\eta = A$ . We obtain the value of the polaron effective mass in the BEC-BCS crossover (Fig. 4).

An important consistency check of our study is provided by the comparison between our direct measurements of  $\eta_c(\delta_1)$  (from Fig. 1, black dots in the inset of Fig. 4) and a calculated  $\eta_c(\delta_1)$  from Eq. 8 and the EoS of the superfluid  $h_S$ . Assuming negligible surface tension, the normal/superfluid boundary is given by equating the pressure and chemical potential in the two phases. This procedure leads to the solid red line in the inset of Fig. 4, in excellent agreement with

the direct measurements. In addition, by integrating our measured EoS of the homogeneous gas over the trap, one retrieves the critical polarization for superfluidity of a trapped gas, in agreement with most previous measurements (6).

We have measured the equation of state of a two-component Fermi gas at zero temperature in the BEC-BCS crossover. Extensions of our work include exploring the thermodynamics of the far BEC region of the phase diagram where a new phase associated with a polarized superfluid appears (17, 26), mapping the EoS as a function of temperature, and investigating the influence of finite interaction range, which is playing a key role in higher-density parts of neutron stars.

#### References and Notes

- M. Inguscio, W. Ketterle, C. Salomon, Eds. *Ultra-cold Fermi Gases: Proceedings of the International School of Physics "Enrico Fermi", Course CLXIV, Varenna, 20 to 30 June 2006* (IOS Press, Amsterdam, 2008).
- A. J. Leggett, in *Modern Trends in the Theory of Condensed Matter*, A. Pekalski, R. Przystawa, Eds. (Springer-Verlag, Berlin, 1980), pp. 13–27.
- Y. Shin, *Phys. Rev. A* **77**, 041603 (2008).
- S. Nascimbène, N. Navon, K. J. Jiang, F. Chevy, C. Salomon, *Nature* **463**, 1057 (2010).
- T. Ho, Q. Zhou, *Nat. Phys.* **6**, 131 (2009).
- Materials and methods are available as supporting material on Science Online.
- S. Nascimbène *et al.*, *Phys. Rev. Lett.* **103**, 170402 (2009).
- Y. Shin, M. Zwierlein, C. Schunck, A. Schirotzek, W. Ketterle, *Phys. Rev. Lett.* **97**, 30401 (2006).
- T. D. Lee, C. N. Yang, *Phys. Rev.* **105**, 1119 (1957).
- R. B. Diener, R. Sensarma, M. Randeria, *Phys. Rev. A* **77**, 023626 (2008).
- G. Baker Jr., *Rev. Mod. Phys.* **43**, 479 (1971).
- H. Hu *et al.*, "Universal structure of a strongly interacting Fermi superfluid," <http://arxiv.org/abs/1001.3200> (2010).
- C. Lobo, I. Carusotto, S. Giorgini, A. Recati, S. Stringari, *Phys. Rev. Lett.* **97**, 100405 (2006).
- S. Tan, *Ann. Phys.* **323**, 2971 (2008).
- X. Leyronas, R. Combescot, *Phys. Rev. Lett.* **99**, 170402 (2007).
- A. Altmeyer *et al.*, *Phys. Rev. Lett.* **98**, 040401 (2007).
- Y. I. Shin, A. Schirotzek, C. H. Schunck, W. Ketterle, *Phys. Rev. Lett.* **101**, 070404 (2008).
- T. Wu, *Phys. Rev.* **115**, 1390 (1959).
- E. Braaten, H. W. Hammer, T. Mehen, *Phys. Rev. Lett.* **88**, 040401 (2002).
- S. Tan, *Phys. Rev. A* **78**, 013636 (2008).
- H. Hu, X. Liu, P. Drummond, *Europhys. Lett.* **74**, 574 (2006).
- A. Bulgac, J. Drut, P. Magierski, *Phys. Rev. A* **78**, 023625 (2008).
- R. Haussmann, W. Rantner, S. Cerrito, W. Zwerger, *Phys. Rev. A* **75**, 023610 (2007).
- S. Chang, V. Pandharipande, J. Carlson, K. Schmidt, *Phys. Rev. A* **70**, 043602 (2004).
- G. E. Astrakharchik, J. Boronat, J. Casulleras, A. S. Giorgini, *Phys. Rev. Lett.* **93**, 200404 (2004).
- S. Pilati, S. Giorgini, *Phys. Rev. Lett.* **100**, 030401 (2008).
- C. Lobo, A. Recati, S. Giorgini, S. Stringari, *Phys. Rev. Lett.* **97**, 200403 (2006).
- A. Schirotzek, C.-H. Wu, A. Sommer, M. W. Zwierlein, *Phys. Rev. Lett.* **102**, 230402 (2009).
- R. Combescot, A. Recati, C. Lobo, F. Chevy, *Phys. Rev. Lett.* **98**, 180402 (2007).
- N. Prokof'ev, B. Svistunov, *Phys. Rev. B* **77**, 020408 (2008).
- R. Combescot, S. Giraud, X. Leyronas, *Europhys. Lett.* **88**, 60007 (2009).
- In the BEC limit, the grand-canonical EoS expands as  $h_S(\tilde{\delta}) \approx 15\pi a/4a_{dd}\tilde{\delta} - 16\sqrt{2}$ ; the first term is the mean-field interaction and the second is the LHY correction asymptotic behavior.
- A. Schirotzek, Y. I. Shin, C. H. Schunck, W. Ketterle, *Phys. Rev. Lett.* **101**, 140403 (2008).
- We thank K. Jiang for participation in the early phase of the experimental work. We are grateful to X. Leyronas, C. Mora, Y. Castin, F. Werner, R. Combescot, J. Dalibard, F. Gerbier, and G. Shlyapnikov for stimulating discussions and critical comments on the manuscript. We thank S. Giorgini, P. Drummond, J. Drut, R. Haussmann, and W. Zwerger for providing us with their data. We acknowledge support from European Research Council, European Science Foundation (Euroquom), SCALA (Scalable Quantum Computing with Light and Atoms), Agence Nationale de la Recherche FABIOLA (Fermions and Bosons in Optical Lattices), Région Ile de France Institut Francilien de Recherche sur les Atomes Froids, and Institut Universitaire de France.

#### Supporting Online Material

[www.sciencemag.org/cgi/content/full/science.1187582/DC1](http://www.sciencemag.org/cgi/content/full/science.1187582/DC1)  
Materials and Methods  
Figs. S1 to S4  
References

27 January 2010; accepted 30 March 2010  
Published online 15 April 2010;  
10.1126/science.1187582  
Include this information when citing this paper.

## Nanoscale Three-Dimensional Patterning of Molecular Resists by Scanning Probes

David Pires,<sup>1</sup> James L. Hedrick,<sup>2</sup> Anuja De Silva,<sup>3</sup> Jane Frommer,<sup>2</sup> Bernd Gotsmann,<sup>1</sup> Heiko Wolf,<sup>1</sup> Michel Despont,<sup>1</sup> Urs Duerig,<sup>1</sup> Armin W. Knoll<sup>1\*</sup>

For patterning organic resists, optical and electron beam lithography are the most established methods; however, at resolutions below 30 nanometers, inherent problems result from unwanted exposure of the resist in nearby areas. We present a scanning probe lithography method based on the local desorption of a glassy organic resist by a heatable probe. We demonstrate patterning at a half pitch down to 15 nanometers without proximity corrections and with throughputs approaching those of Gaussian electron beam lithography at similar resolution. These patterns can be transferred to other substrates, and material can be removed in successive steps in order to fabricate complex three-dimensional structures.

To date, a wide variety of techniques has been available for nanofabrication (1), including electron beam lithography (EBL)

and scanning probe lithography (SPL) (2–4) as direct-write methods. Although EBL is used in critical applications such as the fabrication of